





Modeling the light-powered self-rotation of a liquid crystal elastomer fiber-based engineYong Yu , Haoyu Hu, Yuntong Dai , and Kai Li *
School of Civil Engineering, Anhui Jianzhu University, Hefei 230601, China (Received 16 August 2023; accepted 8 February 2024; published 4 March 2024)

Self-oscillating systems possess the ability to convert ambient energy directly into mechanical work, and new types of self-oscillating systems are worth designing for practical applications in energy harvesters, engines and actuators. Taking inspiration from the four-stroke engine. A concept for a self-rotating engine is presented on the basis of photothermally responsive materials, consisting of a liquid crystal elastomer (LCE) fiber, a hinge and a turnplate, which can self-rotate under steady illumination. Based on the photo-thermal-mechanical model, a nonlinear theoretical model of the LCE-based engine under steady illumination is proposed to investigate its self-rotating behaviors. Numerical calculations reveal that the LCE-based engine experiences a supercritical Hopf bifurcation between the static regime and the self-rotation regime. The self-rotation of the LCE-based engine originates from the photothermally driven strain of the LCE fiber in illumination, and its continuous periodic motion is sustained by the correlation between photothermal energy and damping dissipation. The Hopf bifurcation conditions are also explored in detail, as well as the vital system parameters affecting self-rotation frequency. Compared to the abundant existing self-oscillating systems, this conceptual self-rotating LCE-based engine stands out due to its simple and lightweight structure, customizable dimensions and high speed, and it is expected to offer a broader range of design concepts applicable to soft robotics, energy harvesters, medical instruments, and so on.

DOI: [10.1103/PhysRevE.109.034701](https://doi.org/10.1103/PhysRevE.109.034701)**I. INTRODUCTION**

Self-sustained oscillation is a periodic oscillatory phenomenon triggered by steady external excitations [1], which can be maintained in a continuous periodic manner by means of periodically absorbing energy from constant external stimuli, without the need for additional complex controllers and portable batteries [2–6]. As a result, to a certain extent, the complexity of self-oscillating systems is reduced, and interesting applications including portability become possible [7–13]. Furthermore, the self-oscillation frequency generally depends on the parameters of the system itself and is almost independent of the initial conditions, making the system robust [14,15]. Taking advantage of these benefits in self-oscillation, self-oscillating systems are becoming attractive candidates for a variety of practical applications, including active machines [16–22], autonomous robotics [23], energy-absorbing devices [24–26], motors [27], etc.

On basis of the stimuli-responsive materials such as liquid crystal elastomers (LCEs) [28], ionic gels [29,30], hydrogels [31,32], etc., diverse self-oscillating systems have recently emerged. In particular, numerous attempts have been made to construct a large number of self-sustained motion patterns such as vibration [33], bending [34,35], rolling [36–38], spinning [39], torsion [40], shuttling [41], self-oscillating auxetic metamaterials [42], self-floating [43], self-curling [44], shrinking [45], swimming [46], swinging [16,47], buckling [48,49], jumping [50,51], rotation [52,53], chaos [54], and

even synchronized motion of coupled self-oscillators [55]. For these proposed self-oscillating systems, some special mechanisms are generally required to absorb energy from the external environment to compensate for the energy dissipation consumed by system damping [1]. Given different stimuli-responsive materials, various feedback mechanisms have been proposed to achieve energy compensation [16,17,56], such as the coupling mechanism between chemical reaction and large deformation [29,30], the self-shading mechanism [16,17,57], and the multiprocess coupling mechanism between droplet evaporation and movement [58]. These mechanisms are always accompanied by nonlinear coupling of multiple processes and self-oscillatory feedback [56–58].

Among the stimuli-responsive materials that constitute self-excited oscillatory systems, LCE offers some special benefits. LCE is fabricated by synthesizing anisotropic rodlike liquid crystal molecules and stretchable long-chain polymers [59]. When exposed to environmental stimuli, such as light [21], heat [60], electricity [61], and magnetism [62], the liquid crystal monomer molecules rotate or undergo phase transitions, which change their configurations and thereby produce macroscopic deformations [63]. Among the above external stimuli, optical stimulation is a preferable choice as it allows for remote and noncontact operation. Meanwhile, convenient and precise adjustments of intensity, wavelength, and polarization directions are permitted. In addition, photothermal stimulation offers appealing features of abundant light sources and cleanliness. The photothermally responsive LCE exhibits rapid response, large intrinsic deformation as well as reversible deformation. These special properties allow for inducing feedback in various approaches, resulting in

*Corresponding author: kli@ahjzu.edu.cn

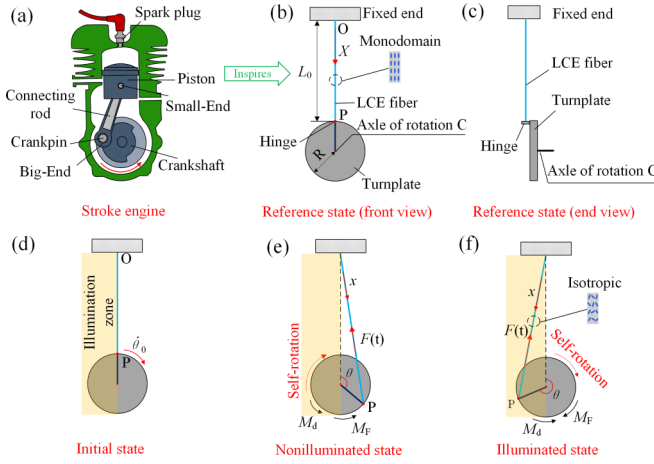


FIG. 1. Schematics of a self-rotating engine, consisting of an LCE fiber, a hinge and a turnplate. (a) Four-stroke engine. (b) Reference state (front view). (c) Reference state (end view). (d) Initial state. (e) Non-illuminated state. (f) Illuminated state. Half of the system is steadily illuminated. The LCE-based engine can maintain a continuous periodic rotation under steady collimated illumination.

light-induced self-sustained oscillations [64], which in turn has led to an extensive practical use of LCE-based light-powered self-oscillating systems [63–65].

Despite the widespread interest in LCE-based self-oscillating systems and the resulting construction of many self-oscillating systems, there is still a need to build self-oscillating systems with more diverse modes of motion to meet the demands of various functional applications. A four-stroke engine is an internal combustion engine that utilizes four distinct piston strokes to complete one operating cycle, and mainly consists of piston, spark plug, crankshaft, and connecting rod. A four-stroke engine undergoes four strokes, i.e., intake, compression, power, and exhaust, to complete an operating cycle. During this period, the piston moves back and forth between the top and bottom dead centers for four strokes, and the crankshaft rotates for two cycles, as shown in Fig. 1(a). Inspired by the four-stroke engine and Knežević’s work [66], a conceptual self-rotating engine is proposed on the basis of photothermally responsive materials, consisting of a LCE fiber, a hinge and a turnplate, which can self-rotate under steady illumination. In contrast to Knežević’s zero-energy-mode engine [66], our proposed LCE-based engine exhibits an unsteady self-rotation with periodically varying angular velocity. The objective of this paper is to present a conceptual photothermally driven self-rotating LCE-based engine, investigate its dynamic behaviors and provide guidance for its practical applications in engineering. This self-rotating system has several unique benefits including simple structure, customizable size, fast speed, and light weight [67–69], and it is expected to present a wider array of design concepts suitable for various applications, including soft robotics, energy harvesters, and medical instruments.

The remainder of this paper is structured as follows. In Sec. II, we first propose a nonlinear dynamic model for the self-rotating LCE-based engine under steady illumination, which involves the well-established dynamic LCE model, and then formulate the corresponding governing equations.

Section III presents the two motion regimes of the LCE-based engine under steady illumination, and discusses the mechanism of self-rotation in detail. In Sec. IV, we focus on the Hopf bifurcation conditions between the static and self-rotation regimes, as well as the influences of various system parameters on the self-rotation frequency. Finally, we conclude our study in Sec. V.

II. MODEL AND FORMULATION

In this section, we first propose a conceptual self-rotating LCE-based engine under steady illumination upon inspiration of Knežević’s work [66] and a four-stroke engine shown in Fig. 1(a). The LCE-based engine, consisting of an LCE fiber, a hinge and a turnplate, is capable of continuous rotation under steady illumination. Taking the photo-thermal-mechanical model into account, a dynamic model for the self-rotating LCE-based engine under steady illumination is established. The main contents include the rotational dynamics of the self-rotating engine, the photothermally driven rotational moment, the tension of the LCE fiber, the nondimensionalization, and the solution method for the differential governing equations with variable coefficients.

A. Dynamics of the LCE-based engine

Figure 1 sketches the conceptual photothermally driven self-rotating LCE-based engine, which consists of an LCE fiber, a hinge and a turnplate. One end of the LCE fiber is connected to the fixed end O , and the other end is connected to point P on the hinge, which is connected to a turnplate with radius R and an axle of rotation C . The LCE fiber utilized is either thiol-acrylate or siloxane LCE, capable of demonstrating significant elastic strains [70]. For the reference state shown in Fig. 1(b), the LCE fiber is stress-free with an original length of L_0 . The LCE fiber is in the monodomain state and liquid crystal mesogens are aligned along the longitudinal direction. The initial state is depicted in Fig. 1(d), with the yellow area representing the collimated illumination zone. Half of the system is steadily illuminated. Initially, the LCE-based engine acquires an initial angular velocity $\dot{\theta}_0$ from the reference state, and the turnplate starts to rotate. At the beginning of the rotation, the LCE fiber has not yet entered the illumination zone [Fig. 1(e)]. Then, as the turnplate rotates to the position with critical rotational angle, $\theta_c = \pi$. When heated up, the LCE fiber contracts along the longitudinal direction due to the transition from the nematic phase to the isotropic phase [Fig. 1(f)].

When the rotational angle of the turnplate is less than the critical angle ($0 \leq \theta \leq \pi$), the tension in the LCE fiber and the corresponding rotational moment tend to rotate the turnplate counterclockwise to its initial state. When the rotational angle of the turnplate exceeds the critical angle ($\pi \leq \theta \leq 2\pi$), the LCE fiber starts to receive steady illumination. Under steady illumination, the tension in the LCE fiber and the corresponding rotational moment increase and tend to continue to rotate the turnplate clockwise, as shown in Fig. 1(e). When passing through the critical position, the turnplate continues to rotate due to its own inertia. Finally, under steady

illumination, the turnplate is able to exhibit continuous periodic rotation.

As described in Fig. 1, the turnplate is subjected to the rotational moment $M_F(t)$ and the damping moment $M_d(t)$. For simplicity, the damping moment $M_d(t)$ is assumed to be proportional to its rotational angular velocity. The corresponding nonlinear dynamic governing equation for the self-rotating engine can be derived as

$$J \frac{d^2\theta(t)}{dt^2} = M_F(t) - \beta \frac{d\theta(t)}{dt}, \quad (1)$$

where β is the damping coefficient and J refers to the moment of inertia of the turnplate about its center point C. In addition, the initial conditions are given as

$$\theta(t) = \theta_0, \quad \frac{d\theta(t)}{dt} = \dot{\theta}_0 \quad \text{at} \quad t = 0. \quad (2)$$

Noted that the rotational moment $M_F(t)$ in Eq. (1) results from the tension of the LCE fiber, which will be calculated in the following.

B. Rotational moment

The rotational moment $M_F(t)$ can be determined from the tension $F(t)$ of the LCE fiber. For the two cases of nonilluminated state ($2n\pi \leq \theta \leq \pi + 2n\pi$) and illuminated state ($\pi + 2n\pi \leq \theta \leq 2\pi + 2n\pi$) during the rotation of the turnplate, there are different analytical expressions for the rotational moment $M_F(t)$. To simplify the formulation, four assumptions are made: (1) the mass of the LCE fiber is negligible; (2) the cross-sectional shape of the LCE fiber remains constant under tension; (3) The friction between LCE fiber is ignored; and (4) the tension is uniform throughout the entire LCE fiber.

(i) Nonilluminated state

For the nonilluminated state, i.e., $2n\pi \leq \theta \leq \pi + 2n\pi$, the rotational moment $M_F(t)$ is closely related to the tension $F(t)$. As depicted in Fig. 1(e), the tension direction of the fiber is along its center line. Referring to the mature model of rigid rotation about a fixed axis [71], the rotational moment $M_F(t)$ in the nonilluminated state is calculated as follows:

$$M_F(t) = -F(t)d. \quad (3)$$

(ii) Illuminated state

For the illuminated state, i.e., $\pi + 2n\pi \leq \theta \leq 2\pi + 2n\pi$, as shown in Fig. 1(f), the rotational moment $M_F(t)$ can be easily calculated as follows:

$$M_F(t) = F(t)d. \quad (4)$$

The length of the LCE fiber $L(t)$ in nonilluminated and illuminated states can be easily obtained from Fig. 1(e) as

$$L(t) = \sqrt{R^2 + (L_0 + R)^2 - 2R(R + L_0) \cos \theta}, \quad (5)$$

and then the moment arm d can be easily obtained as

$$d = \frac{(L_0 + R)R \sin \theta}{L(t)}. \quad (6)$$

C. Tension of the LCE fiber

In order to determine the rotational moment $M_F(t)$ in Eqs. (3) and (4), it is necessary to calculate the tension $F(t)$.

Generally, viscoelasticity of the LCE fiber plays an important role in the rotation of the LCE-based engine. However, for highly crosslinked LCE, it is also reasonable to assume that viscoelasticity is ignored, and the fiber is a linearly elastic material. For simplicity, the friction and mass of the fiber are ignored in the calculations, and the tension $F(t)$ of the fiber is assumed to be proportional to the elastic strain ε_e , i.e.,

$$F(t) = kL_0\varepsilon_e(t), \quad (7)$$

where $k = \frac{EA}{L_0}$ is the spring constant, with E and A being the elastic modulus and the cross area of LCE fiber, respectively. The elastic strain $\varepsilon_e(t)$, the total strain ε_{tot} and the photothermally driven strain ε_L in the LCE fiber are homogeneous and time-dependent. It is noted that the photothermally driven strain can result in net work during one cycle performed by the LCE fiber. This compensation effectively counters damping dissipation, thereby sustaining self-rotation, as elaborated in Sec. III B.

For simplicity, the elastic strain $\varepsilon_e(t)$ under small deformation can be assumed as a linear combination of the total strain $\varepsilon_{\text{tot}}(t)$ and the photothermally driven strain $\varepsilon_L(t)$, i.e., $\varepsilon_{\text{tot}}(t) = \varepsilon_e(t) + \varepsilon_L(t)$. Therefore, the tension can be rewritten as

$$F(t) = kL_0[\varepsilon_{\text{tot}}(t) - \varepsilon_L(t)], \quad (8)$$

$\varepsilon_L(t)$ refers to the photothermally driven strain of LCE with an assumption that it is linearly related to the temperature change $T(t)$ in the LCE fiber and can be written as

$$\varepsilon_L(t) = -C_0T(t), \quad (9)$$

where C_0 is the contraction coefficient. For simplicity, the total strain is defined as $\varepsilon_{\text{tot}}(t) = \frac{L(t) - L_0}{L_0}$. Thus, the tension $F(t)$ in Eq. (8) can be rewritten as

$$F(t) = k\{[L(t) - L_0] + C_0L_0T(t)\}. \quad (10)$$

D. Temperature of the LCE fiber

To calculate the temperature in Eq. (10), this section describes the dynamics of temperature of the photothermally responsive LCE fiber under steady illumination and in dark. During the self-rotation of the LCE-based engine, there is heat exchange between the LCE fiber and the environment. We assume that the radius r of the LCE fiber is much smaller than the length L_0 . For typical values of the heat transfer coefficient $K = 10\text{W/m}^2/\text{K}$, the thermal conductivity $h = 0.1\text{W/m/K}$, and $r = 10^{-5}\text{m}$ in the experiments [72], the Biot number $B_i = Kr/h$ is estimated as $B_i = 10^{-3}$. Therefore, the temperature field in the fiber is nearly homogeneous along its radius. Meanwhile, due to the simultaneous entry of the LCE fiber into the illuminated state or nonilluminated state, the temperature of LCE fiber is assumed to be homogeneous along the longitudinal direction. Under steady illumination, the temperature of LCE fiber can be governed by

$$\frac{dT}{dt} = \frac{q - KT}{\rho_C}, \quad (11)$$

where ρ_C is the specific heat capacity, and q represents the heat flux from the steady illumination.

In this paper, the LCE fiber switches between the illuminated and nonilluminated states. For Case I that the LCE fiber

is in the illuminated state switched from the nonilluminated state with transient temperature T_{dark} , by solving Eq. (11), the temperature T in the LCE fiber is

$$T = T_{\text{dark}} + \frac{q}{K}(1 - e^{-t_1/\tau}) \quad (12)$$

where $\tau = \frac{\rho c}{K}$ denotes the thermal characteristic time, and t_1 is the duration of current process.

For Case II that the LCE fiber is in the nonilluminated state (i.e., $q = 0$) switched from the illuminated state with transient temperature T_{illum} , the temperature T in the LCE fiber can be derived from Eq. (11) as

$$T = T_{\text{illum}}e^{-t_2/\tau} \quad (13)$$

where, t_2 is the duration of the current process.

E. Nondimensionalization

For convenience, the dimensionless quantities are introduced as follows: $\bar{t}_1 = t_1/\tau$, $\bar{t}_2 = t_2/\tau$, $\bar{L} = L/L_0$, $\bar{R} = R/L_0$, $\bar{d} = d/L_0$, $\bar{M}_F = M_F\tau^2/J$, $\bar{F} = FL_0\tau^2/J$, $\bar{\beta} = \beta\tau/J$, $\bar{k} = k\tau^2L_0^2/J$, $\bar{T} = T/T_e$ (T_e is environmental temperature), $\bar{T}_{\text{illum}} = T_{\text{illum}}/T_e$, $\bar{T}_{\text{dark}} = T_{\text{dark}}/T_e$, $\bar{q} = q/KT_e$. In turn, the dimensionless forms for Eqs. (1)–(6), and (10)–(13) can be obtained, as listed below.

The governing equation for the self-rotating LCE-based engine is rewritten as

$$\frac{d^2\theta(\bar{t})}{d\bar{t}^2} = \bar{M}_F(\bar{t}) - \bar{\beta}\frac{d\theta(\bar{t})}{d\bar{t}}, \quad (14)$$

$$\theta(\bar{t}) = \bar{\theta}_0, \quad \frac{d\theta(\bar{t})}{d\bar{t}} = \dot{\bar{\theta}}_0 \quad \text{at} \quad \bar{t} = 0, \quad (15)$$

where $\bar{M}_F(\bar{t})$ is calculated in two cases as for the nonilluminated state ($2n\pi \leq \theta \leq \pi + 2n\pi$),

$$\bar{M}_F(\bar{t}) = -\bar{F}(\bar{t})\bar{d}, \quad (16)$$

and for the illuminated state ($\pi + 2n\pi \leq \theta \leq 2\pi + 2n\pi$),

$$\bar{M}_F(\bar{t}) = \bar{F}(\bar{t})\bar{d}, \quad (17)$$

where $\bar{F}(\bar{t})$ is

$$\bar{F}(\bar{t}) = \bar{k}\{[\bar{L}(\bar{t}) - 1] + C_0T(\bar{t})\}, \quad (18)$$

and the current moment arm d is

$$\bar{d} = \frac{(1 + \bar{R})\bar{R} \sin \theta}{\bar{L}(\bar{t})}. \quad (19)$$

The current fiber length $\bar{L}(\bar{t})$ for nonilluminated and illuminated states can be expressed as

$$\bar{L}(\bar{t}) = \sqrt{\bar{R}^2 + (1 + \bar{R})^2 - 2\bar{R}(\bar{R} + 1) \cos \theta}. \quad (20)$$

In addition, for case I, the temperature T in the LCE fiber is

$$\bar{T} = \bar{T}_{\text{dark}} + \bar{q}(1 - e^{-\bar{t}_1}) \quad (21)$$

and for case II, the temperature T in the LCE fiber is

$$\bar{T} = \bar{T}_{\text{illum}}e^{-\bar{t}_2} \quad (22)$$

Equations (14), (21), and (22) govern the self-rotation of LCE-based engine under steady illumination, in which the

TABLE I. Material properties and geometric parameters.

Parameter	Definition	Value	Unit
β	Damping coefficient	0 ~ 0.001	mg · mm ² /s
C_0	Contraction coefficient [73]	0 ~ 0.3	/
q	Heat flux [74]	0–7 × 10 ⁻³	J/s
τ	Thermal characteristic time [74]	1 ~ 100	ms
J	Moment inertia of turnplate	0 ~ 1	mg · mm ²
K	Heat transfer coefficient [75]	1	W/m ² · K
L_0	Original length of LCE fiber	1	m
k	Spring constant of LCE fiber	9.5	N/m
R	Radius of turnplate	0.05	m
ρc	Specific heat capacity	0.1	J/kg · K
T_e	Ambient temperature	300	K

time-dependent temperature is coupled with the angular position of the LCE-based engine. In order to solve these complex differential equations with variable coefficients, the fourth-order Runge-Kutta method is used and numerical calculations are carried out in MATLAB software. For the temperature \bar{T}_i and the position θ_i of LCE-based engine at time \bar{t}_i , the current tension \bar{F}_i of LCE fiber and the current rotational moment \bar{M}_{Fi} can be determined from Eqs. (16) to (20). Then the angular position θ_{i+1} at \bar{t}_{i+1} can be calculated from Eq. (14). Meanwhile, the current temperature \bar{T}_i are determined to estimate the heat flux \bar{q} from Eqs. (21) and (22). Thus, the dynamic of self-rotating LCE-based engine can be numerically obtained through iteration calculation for given parameters C_0 , \bar{q} , $\bar{\beta}$, \bar{k} , $\dot{\bar{\theta}}_0$, \bar{R} .

III. TWO MOTION REGIMES AND MECHANISM OF SELF-ROTATION

In this section, based on the solution of the governing Eqs. (15) and (22), we first introduce two typical motion regimes of the LCE-based engine, i.e., the static regime and the self-rotation regime. Next, the corresponding mechanism of self-rotation is investigated in detail.

A. Two motion regimes

To investigate the self-rotating LCE-based engine under steady illumination, the typical values for the dimensionless parameters in the model should be determined first. From the available experiments [73–75], the typical material properties and geometric parameters are listed in Table I. The corresponding dimensionless parameters are also listed in Table II. Among these parameters, C_0 , τ , and K are the key parameters, which are set according to the related experiments [73–75]. In practice, other geometric and physical parameters can be easily tuned. It is noted that recent experiments have shown

TABLE II. Dimensionless parameters.

Parameter	θ_0	$\dot{\bar{\theta}}_0$	$\bar{\beta}$	\bar{q}	C_0	\bar{k}	\bar{R}
Value	0 ~ 10	0 ~ 10	0 ~ 0.1	0 ~ 0.7	0 ~ 0.3	0 ~ 40	0 ~ 0.05

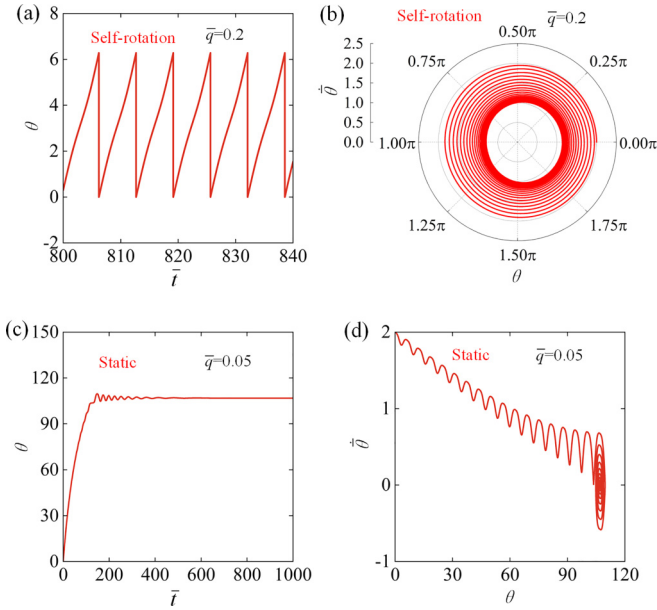


FIG. 2. Time histories and phase trajectories for the two motion regimes of the LCE-based engine. (a) and (b) are the self-rotation regime with $\bar{q} = 0.2$; (c) and (d) are the static regime with $\bar{q} = 0.05$. The other parameters are $C_0 = 0.3$, $\bar{k} = 40$, $\bar{\beta} = 0.02$, $\theta_0 = 0$, $\bar{R} = 0.05$, and $\dot{\theta}_0 = 2$. The LCE-based engine under steady illumination can develop into two motion regimes: the static regime and the self-rotation regime, which means that the engine experiences a supercritical Hopf bifurcation as described in Sec. IV.

that the thermal characteristic time of the LCE fiber to photothermal stimulation is less than 10^{-1} s, and several instances of self-oscillations have been successfully showcased [76,77].

By numerically solving Eqs. (16)-(21), the time histories and phase trajectories of self-rotation can be obtained, among which the cases for $\bar{q} = 0.2$ and $\bar{q} = 0.05$ are shown in Fig. 2 and Video 1 in the Supplemental Material [78]. In the calculation, we set the other parameters as $C_0 = 0.3$, $\bar{k} = 40$, $\bar{\beta} = 0.02$, $\theta_0 = 0$, $\bar{R} = 0.05$, and $\dot{\theta}_0 = 2$. For $\bar{q} = 0.2$, the LCE-based engine starts to rotate from rest, and the rotation frequency gradually tends to stabilize. Finally, under steady illumination, the LCE-based engine presents a continuous periodic rotation, which we refer to as the self-rotation regime [Figs. 2(a) and 2(b)]. For $\bar{q} = 0.05$, the rotation frequency of the LCE-based engine exhibits a gradual increase with time due to the damping dissipation, and the LCE-based engine eventually attains stationary at the equilibrium position, which is named as the static regime [Figs. 2(c) and 2(d)]. This result implies that the engine experiences a supercritical Hopf bifurcation as discussed in Sec. IV. Next, we will further investigate the mechanism of self-rotation in detail.

B. Mechanism of self-rotation

To investigate the mechanism of self-rotation, Fig. 3 illustrates several important physical quantities of the LCE-based engine for the typical case shown in Figs. 2(a) and 2(b). Figure 3(a) plots the time history curve of the temperature \bar{T} , reflecting its periodic variation with time. As the LCE fiber enters the illumination zone, the temperature \bar{T} increases and

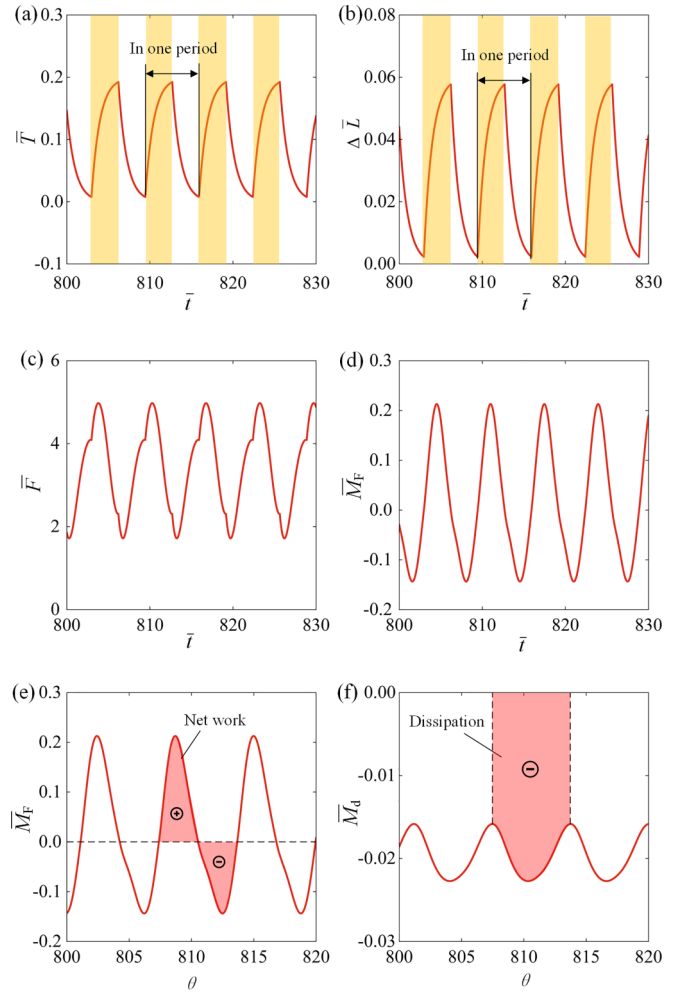


FIG. 3. Mechanism of the self-rotation for the typical case in 3 (a) and (b). (a) Time history curve of the temperature \bar{T} in the LCE fiber. (b) Time history curve of the photothermally induced fiber length change $\Delta \bar{L}$. (c) Time history curve of the tension of the LCE fiber. (d) Time history curve of the rotational moment \bar{M}_F . (e) Relationship between rotational moment \bar{M}_F and angular position θ . The rotational moment \bar{M}_F is jointly determined by tension \bar{F} and angular position θ , as expressed in Eqs. (16), (17), and (19). The area enclosed by the curve in Fig. 3(e) represents the positive net work done by the LCE fiber, which is numerically calculated to be 0.12385. Figure 3(f) shows the relationship between damping moment \bar{M}_d and angular position θ , with the area enclosed by the curve representing the damping dissipation, which is numerically calculated to be 0.12385. The net work done by the LCE fiber is exactly identical to the damping dissipation, implying that the

approaches the maximum value, while it decreases gradually in the dark zone. Figures 3(b) and 3(c), respectively present the time history curves for the fiber length change $\Delta \bar{L}$ and the tension \bar{F} of the LCE fiber induced purely by illumination, both of which exhibit periodic behaviors due to the periodic change in temperature \bar{T} . Figure 3(d) depicts the time history curve of rotational moment \bar{M}_F . Figure 3(e) further reveals the relationship between rotational moment \bar{M}_F and angular position θ . The rotational moment \bar{M}_F is jointly determined by tension \bar{F} and angular position θ , as expressed in Eqs. (16), (17), and (19). The area enclosed by the curve in Fig. 3(e) represents the positive net work done by the LCE fiber, which is numerically calculated to be 0.12385. Figure 3(f) shows the relationship between damping moment \bar{M}_d and angular position θ , with the area enclosed by the curve representing the damping dissipation, which is numerically calculated to be 0.12385. The net work done by the LCE fiber is exactly identical to the damping dissipation, implying that the

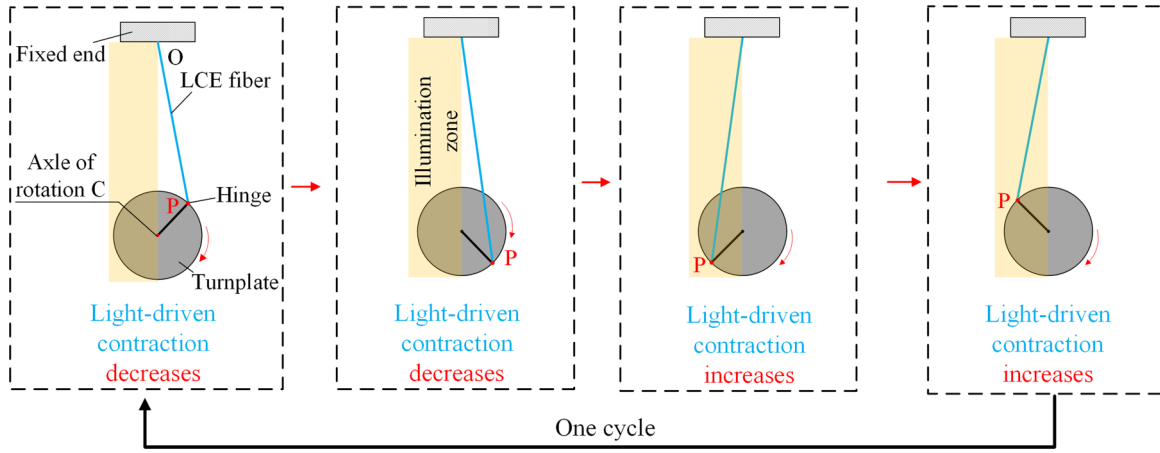


FIG. 4. Snapshots of the self-rotation of the LCE-based engine within one cycle for the typical case in Figs. 2(a) and 2(b). Under steady illumination, the LCE-based engine will exhibit a continuous periodic rotation.

self-rotation results from the competition between the net work done by the LCE fiber and the damping dissipation. Figure 4 depicts the movement of the LCE-based engine over one cycle.

IV. INFLUENCES OF SYSTEM PARAMETERS ON THE SELF-ROTATION

In the above mechanical model of the self-rotation, there are six dimensionless system parameters, including C_0 , \bar{k} , \bar{q} , $\bar{\beta}$, \bar{R} , and $\bar{\theta}_0$. The current section will focus on the influences of these system parameters on the Hopf bifurcation conditions and the frequency of self-rotation.

A. Influence of heat flux

Figure 5 and Video 2 [78] describe the influence of heat flux \bar{q} on the self-rotation of the LCE-based engine. In the calculation, we set $C_0 = 0.3$, $\bar{k} = 40$, $\bar{\theta}_0 = 2$, $\bar{\beta} = 0.02$, $\bar{R} = 0.05$, and $\bar{\theta}_0 = 0$. There exists a critical heat flux of approximately 0.06 to trigger the self-rotation, which indicates that the LCE-based engine experiences a supercritical Hopf bifurcation at the critical heat flux. When $\bar{q} \leq 0.06$, the engine

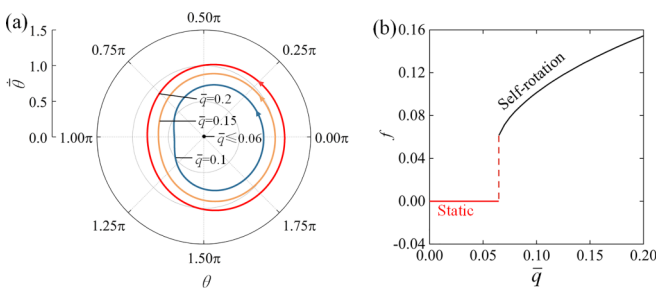


FIG. 5. Influence of heat flux on the self-rotation, for $C_0 = 0.3$, $\bar{k} = 40$, $\bar{\theta}_0 = 2$, $\bar{\beta} = 0.02$, $\bar{R} = 0.05$, and $\bar{\theta}_0 = 0$. (a) Limit cycles. (b) Frequency variation with heat flux. There exists a critical heat flux of $\bar{q} \approx 0.06$ for the supercritical Hopf bifurcation between the static regime and the self-rotation regime. With the increase of heat flux \bar{q} , the frequency of self-rotation presents an upward trend.

always stops at an equilibrium position, referring to a static regime, whereas the self-rotation regime can be triggered when $\bar{q} = 0.1, 0.15, 0.2$. Figure 5(a) plots the limit cycles, while Fig. 5(b) presents the influence of heat flux \bar{q} on the self-rotation frequency. The frequency increases significantly with the increasing heat flux. Self-rotation is the result of light energy being absorbed and converted into mechanical energy, and as the heat flux increases, the more energy is converted, resulting in a shorter duration of self-rotation within one cycle.

B. Influence of contraction coefficient

Figure 6 and Video 3 [78] illustrate the influence of contraction coefficient C_0 on the self-rotation of the LCE-based engine. In the calculation, we set $\bar{q} = 0.2$, $\bar{k} = 40$, $\bar{\theta}_0 = 2$, $\bar{\beta} = 0.02$, $\bar{R} = 0.05$, and $\bar{\theta}_0 = 0$. Similarly, the critical contraction coefficient C_0 for the supercritical Hopf bifurcation is found to be approximately 0.1. The LCE-based engine remains static when $C_0 \leq 0.1$, and for $C_0 = 0.2, 0.25, 0.3$, the self-rotation can be triggered, with their limit cycles being depicted in Fig. 6(a). Figure 6(b) displays the variation of

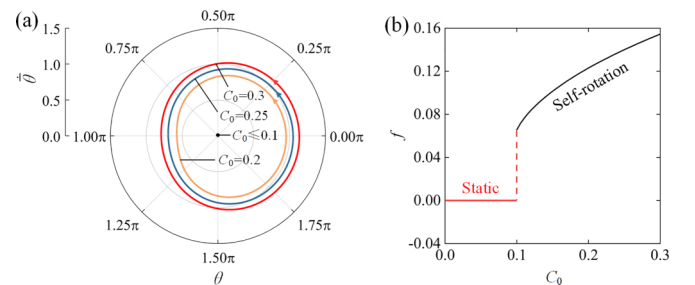


FIG. 6. Influence of contraction coefficient on the self-rotation, for $\bar{q} = 0.2$, $\bar{k} = 40$, $\bar{\theta}_0 = 2$, $\bar{\beta} = 0.02$, $\bar{R} = 0.05$, and $\bar{\theta}_0 = 0$. (a) Limit cycles. (b) Frequency variation with contraction coefficient. A critical contraction coefficient of $C_0 \approx 0.1$ is present for the supercritical Hopf bifurcation between the static regime and the self-rotation regime. As the contraction coefficient C_0 increases, the frequency of self-rotation tends to increase.

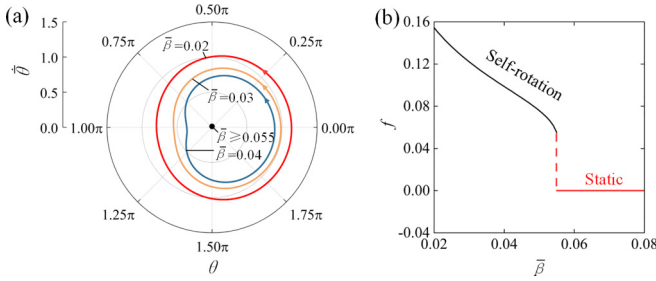


FIG. 7. Influence of damping coefficient on the self-rotation, for $\bar{q} = 0.2$, $\bar{k} = 40$, $\dot{\bar{\theta}}_0 = 2$, $C_0 = 0.3$, $\bar{R} = 0.05$, and $\bar{\theta}_0 = 0$. (a) Limit cycles. (b) Frequency variation with damping coefficient. A critical damping coefficient of $\bar{\beta} \approx 0.055$ exists for the supercritical Hopf bifurcation between the static regime and the self-rotation regime. The increase of damping coefficient $\bar{\beta}$ results in the decline of the self-rotation frequency.

self-rotation frequency with contraction coefficient. As the contraction coefficient C_0 increases, the frequency tends to increase. Equation (9) provides evidence that increasing the contraction coefficient leads to an increase in the photothermally driven strain, which corresponds to an increase in the absorbed photothermal energy. This implies that increasing the contraction coefficient of LCE material can enhance the effective conversion of photothermal energy into mechanical energy.

C. Influence of damping coefficient

The influence of damping coefficient $\bar{\beta}$ on the self-rotation of the LCE-based engine is presented in Fig. 7 and Video 4 [78]. Figure 7(a) depicts the limit cycles for different damping coefficients, while Fig. 7(b) expresses the self-rotation frequency as a function of damping coefficient $\bar{\beta}$. In the calculation, the other parameters are set as $\bar{q} = 0.2$, $\bar{k} = 40$, $\dot{\bar{\theta}}_0 = 2$, $C_0 = 0.3$, $\bar{R} = 0.05$, and $\bar{\theta}_0 = 0$. The critical value of damping coefficient $\bar{\beta}$ for the supercritical Hopf bifurcation is approximately equal to 0.055. When $\bar{\beta} \geq 0.055$, the energy dissipation due to damping is too large and the energy input from the external environment is not sufficient to compensate for this dissipation, resulting in a static regime. However, for $\bar{\beta} = 0.02$, $\bar{\beta} = 0.03$, and $\bar{\beta} = 0.04$, the self-rotation regime can be triggered. An increase in the damping coefficient leads to a decrease in the frequency of self-rotation. According to the previous derivation, the larger the damping coefficient, the more energy dissipation occurs, leading to an increase in frequency and a longer duration of self-rotation within one cycle.

D. Influence of spring constant

Figure 8 and Video 5 [78] describe the influence of spring constant \bar{k} on the self-rotation of the LCE-based engine. The limit cycles for different spring constants are plotted in Fig. 8(a), while Fig. 8(b) represents the functional relationship between spring constant \bar{k} and self-rotation frequency. In the calculation, we set the other parameters as $\bar{q} = 0.2$, $\bar{\beta} = 0.02$, $\dot{\bar{\theta}}_0 = 2$, $C_0 = 0.3$, $\bar{R} = 0.05$, and $\bar{\theta}_0 = 0$. A critical value of

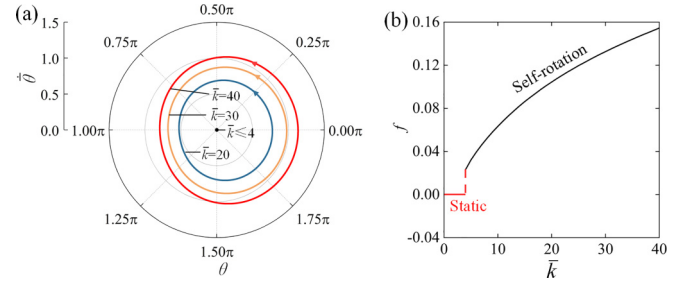


FIG. 8. Influence of spring constant on the self-rotation, for $C_0 = 0.3$, $\bar{\beta} = 0.02$, $\bar{q} = 0.2$, $\bar{\theta}_0 = 0$, $\bar{R} = 0.05$, and $\dot{\bar{\theta}}_0 = 2$. (a) Limit cycles. (b) Frequency variation with spring constant. There is a critical spring constant of $\bar{k} \approx 4$ for the supercritical Hopf bifurcation between the static regime and the self-rotation regime. With the increase of spring constant \bar{k} , the frequency of self-rotation displays an increasing trend.

spring constant \bar{k} approximately equal to 4 is present for the supercritical Hopf bifurcation. When $\bar{k} \leq 4$, the lower tension of the LCE fiber results in smaller net work done by the rotational moment, and therefore cannot compensate for the damping dissipation to maintain the self-rotation. The increasing trend of self-rotation frequency as the spring constant \bar{k} increases is depicted in Fig. 8(b). Given the above derivation, the tension and rotational moment of the LCE fiber also increase with the increasing spring constant \bar{k} , leading to an increase in the net work done by the rotational moment in one cycle. Considering the physical significance of spring constant \bar{k} , increasing the spring constant of the LCE fiber helps to improve the efficiency of converting photothermal energy into mechanical energy for engineering applications.

E. Influence of turnplate radius

The influence of turnplate radius \bar{R} on the self-rotation of the LCE-based engine is presented in Fig. 9 and Video 6 [78]. Figure 9(a) provides the limit cycles for different turnplate radius, and the frequency variation with turnplate radius is plotted in Fig. 9(b). In the calculation, we set $\bar{q} = 0.2$,

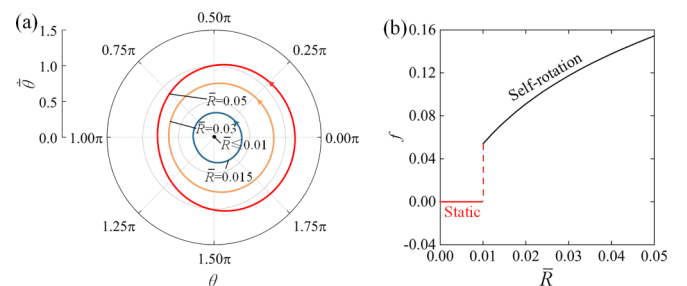


FIG. 9. Influence of turnplate radius on the self-rotation, for $C_0 = 0.3$, $\bar{k} = 40$, $\bar{q} = 0.2$, $\bar{\beta} = 0.02$, $\bar{\theta}_0 = 0$, and $\dot{\bar{\theta}}_0 = 2$. (a) Limit cycles. (b) Frequency variation with turnplate radius. A critical turnplate radius of $\bar{R} \approx 0.01$ is present for the supercritical Hopf bifurcation between the static regime and the self-rotation regime. As the turnplate radius \bar{R} increases, the frequency of self-rotation increases.

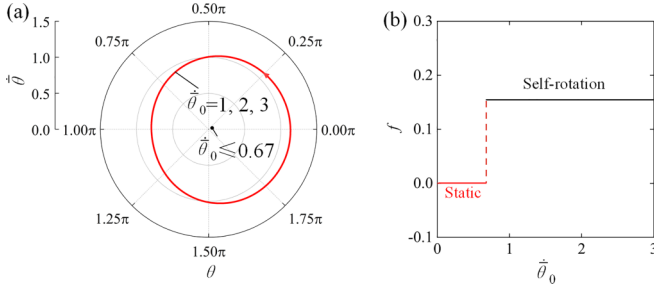


FIG. 10. Influence of initial velocity on the self-rotation, for $C_0 = 0.3$, $\bar{k} = 40$, $\bar{q} = 0.2$, $\bar{\beta} = 0.02$, $\bar{R} = 0.05$, and $\bar{\theta}_0 = 0$. (a) Limit cycles. (b) Frequency variation with initial velocity. A critical initial velocity of $\dot{\bar{\theta}}_0 \approx 0.67$ exists for triggering the self-rotation, while the initial velocity $\bar{\theta}_0$ has no effect on the frequency of self-rotation.

$\bar{\beta} = 0.02$, $\dot{\bar{\theta}}_0 = 2$, $C_0 = 0.3$, $\bar{k} = 40$, and $\bar{\theta}_0 = 0$. A critical value of turnplate radius \bar{R} approximately equal to 0.01 exists for the supercritical Hopf bifurcation. When $\bar{R} \leq 0.01$, the smaller turnplate radius induces smaller rotational moment, which in turn results in smaller net work done by the rotational moment, and hence an inability to compensate for the damping dissipation to maintain the self-rotation. Figure 9(b) gives the increasing variation of self-rotation frequency with the increasing turnplate radius \bar{R} . It is evident from Eqs. (16)-(20) that the rotational moment \bar{M}_F increases with the increase of turnplate radius \bar{R} . This finding suggests that increasing the turnplate radius facilitates the improvement in the self-rotation of the LCE-based engine under steady illumination.

F. Influence of initial velocity

Figure 10 and Video 7 [78] show the influence of initial velocity $\dot{\bar{\theta}}_0$ on the self-rotation of the LCE-based engine. In the calculation, the other parameters are set to $C_0 = 0.3$, $\bar{k} = 40$, $\bar{q} = 0.2$, $\bar{\beta} = 0.02$, $\bar{R} = 0.05$, and $\bar{\theta}_0 = 0$. Figure 10(a) plots the limit cycle with different initial velocities and Fig. 10(b) provides the relationship between the frequency of self-rotation and initial velocity $\dot{\bar{\theta}}_0$. A critical initial velocity $\dot{\bar{\theta}}_0$ of approximately 0.67 exists in the phase transition between the static regime and the self-rotation regime. The self-rotation regime is triggered at initial velocities of 1, 2, 3. Clearly observed that the initial velocity has no effect on the limit cycle and the frequency of self-rotation. Considering the equivalence of kinetic energy and potential energy in the conversion, the initial conditions $\bar{\theta}_0$ always have no effect on the frequency of self-rotation, which is an inherent property of self-oscillation [36].

V. CONCLUSIONS

Self-oscillating systems have the ability to continuously convert ambient energy into mechanical work. The design

of more self-oscillating systems lays the foundation for their widespread applications in engineering. Taking inspiration from the four-stroke engine, a conceptual self-rotating engine is proposed on the basis of photothermally responsive materials, consisting of a LCE fiber, a hinge and a turnplate, which can self-rotate under collimated steady illumination. Taking into account the photo-thermal-mechanical model, we propose a theoretical framework for the LCE-based engine under steady collimated illumination to investigate its self-oscillatory behaviors. Numerical calculations demonstrate that the LCE-based engine experiences a supercritical Hopf bifurcation between the static regime and the self-rotation regime. The self-rotation of the LCE-based engine can be interpreted as the photothermally driven strain of the LCE fiber under illumination. Attributed to the competition between photothermal energy and damping dissipation, it behaves in a continuous periodic manner.

Furthermore, the frequency of self-rotation depends primarily on several system parameters. Increasing the system parameters, including turnplate radius \bar{R} , contraction coefficient C_0 , heat flux \bar{q} and spring constant \bar{k} , can improve the self-rotation frequency, while an increase in damping coefficient $\bar{\beta}$ leads to a decrease in the self-rotation frequency. These qualitative behaviors of the self-rotating LCE-based engine revealed by the model in current article are consistent with physical intuition. In practice, various complex factors can contribute to quantitative deviations from the actual conditions. These factors include the inertia of the LCE fiber, the nonlinear constitutive law, the viscoelastic properties, the bending stiffness, as well as the friction between the fiber, the hinge, and the turnplate. Hence, it is important to account for these factors to accurately capture the actual behavior and performance of the system.

It is worthwhile to further validate the self-rotation behaviors by designing a prototype of the LCE-based engine in future work. To diminish the deviations of the experimental results from the ideal theoretical situation, the LCE fiber in the experiment should be thin enough to reduce its own inertia and bending stiffness. It is also recommended to fabricate LCE fibers with larger contraction coefficient and to utilize larger heat flux in experiments. In addition, the friction of the turnplate should be very small to reduce the damping dissipation so as to trigger the self-rotation. The conceptual self-rotating LCE-based engine proposed in current paper presents superiority in terms of ease of preparation, lightweight structure, customizable dimension and rapid response, and it is expected to offer a broader range of design concepts applicable to soft robotics, energy harvesters, medical instruments, and so on.

ACKNOWLEDGMENTS

This study was supported by University Natural Science Research Project of Anhui Province (Grant No. 2022AH020029), National Natural Science Foundation of China (Grants No. 12202002 and No. 12172001), and Anhui Provincial Natural Science Foundation (Grants No. 2208085Y01 and No. 2008085QA23).

- [1] A. Jenkins, Self-oscillation, *Phys. Rep.* **525**, 167 (2013).
- [2] K. Korner, A. S. Kuenstler, R. C. Hayward, B. Audoly, and K. Bhattacharya, A nonlinear beam model of photomotile structures, *P. Natl. Acad. Sci. USA* **117**, 9762 (2020).
- [3] S. Li, H. Peng, C. Liu, C. Ding, and H. Tang, Nonlinear characteristic and chip breaking mechanism for an axial low-frequency self-excited vibration drilling robot, *Int. J. Mech. Sci.* **230**, 107561 (2022).
- [4] J. Niehues, G. G. Jensen, and J. O. Haerter, Self-organized quantization and oscillations on continuous fixed-energy sandpiles, *Phys. Rev. E* **105**, 034314 (2022).
- [5] X. Wang and G. W. Ho, Design of untethered soft material micromachine for life-like locomotion, *Mater. Today* **53**, 197 (2022).
- [6] Z. Zhang, N. Duan, C. Lin, and H. Hua, Coupled dynamic analysis of a heavily-loaded propulsion shafting system with continuous bearing-shaft friction, *Int. J. Mech. Sci.* **172**, 105431 (2020).
- [7] W. Hu, G. Z. Lum, M. Mastrangeli, and M. Sitti, Small-scale soft-bodied robot with multimodal locomotion, *Nature (London)* **554**, 81 (2018).
- [8] H. Huang and T. Aida, Towards molecular motors in unison, *Nat. Nanotechnol.* **14**, 407 (2019).
- [9] D. Martella, S. Nocentini, C. Parmeggiani, and D. S. Wiersma, Self-regulating capabilities in photonic robotics, *Adv. Mater. Tech.* **4**, 1800571 (2019).
- [10] K. Kruse and F. Jülicher, Oscillations in cell biology, *Curr. Opin. Cell Biol.* **17**, 20 (2005).
- [11] B. Shin, J. Ha, M. Lee, K. Park, G. H. Park, T. H. Choi, K. J. Cho, and H. Y. Kim, Hygrobot: A self-locomotive ratcheted actuator powered by environmental humidity, *Sci. Robot* **3**, eaar2629 (2018).
- [12] P. Rothemund, A. Ainla, L. Belding, D. J. Preston, S. Kurihara, Z. Suo, and G. M. Whitesides, A soft bistable valve for autonomous control of soft actuators, *Sci. Robot* **3**, eaar7986 (2018).
- [13] Z. Li, N. V. Myung, and Y. Yin, Light-powered soft steam engines for self-adaptive oscillation and biomimetic swimming, *Sci. Robot* **6**, eabi4523 (2021).
- [14] V. Sangwan, A. Taneja, and S. Mukherjee, Design of a robust self-excited biped walking mechanism, *Mech. Mach. Theory* **39**, 1385 (2004).
- [15] S. Chatterjee, Self-excited oscillation under nonlinear feedback with time-delay, *J. Sound Vib.* **330**, 1860 (2011).
- [16] S. Serak, N. V. Tabiryan, R. Vergara, T. J. White, R. A. Vaia, and T. J. Bunning, Liquid crystalline polymer cantilever oscillators fueled by light, *Soft Matter* **6**, 779 (2010).
- [17] H. Zeng, M. Lahikainen, L. Liu, Z. Ahmed, O. M. Wani, M. Wang, and A. Priimagi, Light-fuelled freestyle self-oscillators, *Nat. Commun.* **10**, 5057 (2019).
- [18] T. J. White, N. V. Tabiryan, S. V. Serak, U. A. Hrozhyk, V. P. Tondiglia, H. Koerner, R. A. Vaia, and T. J. Bunning, A high frequency photodriven polymer oscillator, *Soft Matter* **4**, 1796 (2008).
- [19] C. Ahn, K. Li, and S. Cai, Light or thermally powered autonomous rolling of an elastomer rod, *ACS Appl. Mater. Inter.* **10**, 25689 (2018).
- [20] X. Lu, H. Zhang, G. Fei, B. Yu, X. Tong, H. Xia, and Y. Zhao, Liquid-crystalline dynamic networks doped with gold nanorods showing enhanced photocontrol of actuation, *Adv. Mater.* **30**, 1706597 (2018).
- [21] Y. Cheng, H. Lu, X. Lee, H. Zeng, and A. Priimagi, Kirigami-based light-induced shape-morphing and locomotion, *Adv. Mater.* **32**, 1906233 (2019).
- [22] Y. Kageyama, T. Ikegami, S. Satonaga, K. Obara, H. Sato, and S. Takeda, Light-driven flipping of azobenzene assemblies-sparse crystal structures and responsive behavior to polarized light, *Chem. Eur. J.* **26**, 10759 (2020).
- [23] M. Wehner, R. L. Truby, D. J. Fitzgerald, B. Mosadegh, G. M. Whitesides, J. A. Lewis, and R. J. Wood, An integrated design and fabrication strategy for entirely soft, autonomous robots, *Nature (London)* **536**, 451 (2016).
- [24] S. Chun, C. Pang, and S. B. Cho, A micropillar-assisted versatile strategy for highly sensitive and efficient triboelectric energy generation under in-plane stimuli, *Adv. Mater.* **32**, 1905539 (2020).
- [25] R. Tang, Z. Liu, D. Xu, J. Liu, L. Yu, and H. Yu, Optical pendulum generator based on photomechanical liquid-crystalline actuators, *ACS Appl. Mater. Inter.* **7**, 8393 (2015).
- [26] D. Zhao and Y. Liu, A prototype for light-electric harvester based on light sensitive liquid crystal elastomer cantilever, *Energy* **198**, 117351 (2020).
- [27] M. Yamada, M. Kondo, J. Mamiya, Y. Yu, M. Kinoshita, C. J. Barrett, and T. Ikeda, Photomobile polymer materials: Towards light-driven plastic motors, *Angew. Chem.* **47**, 4986 (2008).
- [28] M. Lahikainen, H. Zeng, and A. Priimagi, Reconfigurable photoactuator through synergistic use of photochemical and photothermal effects, *Nat. Commun.* **9**, 4148 (2018).
- [29] J. Boissonade and P. D. Kepper, Multiple types of spatio-temporal oscillations induced by differential diffusion in the Landolt reaction, *Phys. Chem. Chem. Phys.* **13**, 4132 (2011).
- [30] K. Li, P. Y. Wu, and S. Cai, Chemomechanical oscillations in a responsive gel induced by an autocatalytic reaction, *J. Appl. Phys.* **116**, 043523 (2014).
- [31] V. V. Yashin and A. C. Balazs, Pattern formation and shape changes in self-oscillating polymer gels, *Science* **314**, 798 (2006).
- [32] X. He, M. Aizenberg, O. Kuksenok, L. D. Zarzar, A. Shastri, A. C. Balazs, and J. Aizenberg, Synthetic homeostatic materials with chemo-mechano-chemical selfregulation, *Nature (London)* **487**, 214 (2012).
- [33] M. Cunha, A. R. Peeketi, A. Ramgopal, R. K. Annabattula, and A. Schenning, Light-driven continual oscillatory rocking of a polymer film, *ChemistryOpen* **9**, 1149 (2020).
- [34] Y. Hu, Q. Ji, M. Huang, L. Chang, C. Zhang, G. Wu, B. Zi, N. Bao, W. Chen, and Y. Wu, Light-driven self-oscillating actuators with pototactic locomotion based on black phosphorus heterostructure, *Angew. Chem. Int. Ed.* **60**, 20511 (2021).
- [35] J. Sun, W. Hu, L. Zhang, R. Lan, H. Yang, and D. Yang, Light-driven self-oscillating behavior of liquid-crystalline networks triggered by dynamic isomerization of molecular motors, *Adv. Funct. Mater.* **31**, 2103311 (2021).
- [36] B. Liao, H. Zang, M. Chen, Y. Wang, X. Lang, N. Zhu, Z. Yang, and Y. Yi, Soft rod-climbing robot inspired by winding locomotion of snake, *Soft Robot* **7**, 500 (2020).

- [37] A. Bazir, A. Baumann, F. Ziebert, and I. M. Kulić, Dynamics of fiberboids, *Soft Matter* **16**, 5210 (2020).
- [38] X. Su, K. Li, W. Hu, and P. Xu, Self-sustained rolling of a liquid crystal elastomer rod under inclined light illumination, *Int. J. Mech. Sci.* **226**, 107411 (2022).
- [39] D. Ge, Y. Dai, and K. Li, Light-powered self-spinning of a button spinner, *Int. J. Mech. Sci.* **238**, 107824 (2023).
- [40] Y. Zhao, Y. Chi, Y. Hong, Y. Li, S. Yang, and J. Yin, Twisting for soft intelligent autonomous robot in unstructured environments, *P. Natl. Acad. Sci. USA* **119**, e2200265119 (2022).
- [41] Y. Yu, C. Du, K. Li, and S. Cai, Controllable and versatile self-motivated motion of a fiber on a hot surface, *Extreme Mech. Lett.* **57**, 101918 (2022).
- [42] L. Zhou, Y. Dai, J. Fang, and K. Li, Light-powered self-oscillation in liquid crystal elastomer auxetic metamaterials with large volume change, *Int. J. Mech. Sci.* **254**, 108423 (2023).
- [43] Q. Cheng, W. Cheng, Y. Dai, and K. Li, Self-oscillating floating of a spherical liquid crystal elastomer balloon under steady illumination, *Int. J. Mech. Sci.* **241**, 107985 (2023).
- [44] J. Liu, J. Zhao, H. Wu, Y. Dai, and K. Li, Self-oscillating curling of a liquid crystal elastomer beam under steady light, *Polymers* **15**, 344 (2023).
- [45] L. Zhou, C. Du, W. Wang, and K. Li, A thermally-responsive fiber engine in a linear temperature field, *Int. J. Mech. Sci.* **225**, 107391 (2022).
- [46] K. Li, Z. Chen, and P. Xu, Light-propelled self-sustained swimming of a liquid crystal elastomer torus at low Reynolds number, *Int. J. Mech. Sci.* **219**, 107128 (2022).
- [47] X. Liang, Z. Chen, L. Zhu, and K. Li, Light-powered self-excited oscillation of a liquid crystal elastomer pendulum, *Mech. Syst. Signal. Pr.* **163**, 108140 (2022).
- [48] D. Ge and K. Li, Self-oscillating buckling and postbuckling of a liquid crystal elastomer disk under steady illumination, *Int. J. Mech. Sci.* **221**, 107233 (2022).
- [49] D. Ge, Y. Dai, and K. Li, Self-sustained euler buckling of an optically responsive rod with different boundary constraints, *Polymers* **15**, 316 (2023).
- [50] P. Xu, J. Jin, and K. Li, Light-powered self-excited bouncing of a liquid crystal elastomer ball, *Int. J. Mech. Sci.* **208**, 106686 (2021).
- [51] D. Ge, J. Jin, Y. Dai, P. Xu, and K. Li, Self-jumping of a liquid crystal elastomer balloon under steady illumination, *Polymers* **14**, 2770 (2022).
- [52] Q. Cheng, X. Liang, and K. Li, Light-powered self-excited motion of a liquid crystal elastomer rotator, *Nonlinear Dyn.* **103**, 2437 (2021).
- [53] T. Sun, K. Li, Y. Dai, and J. Zhao, Self-oscillation and self-rotation of an optically-responsive liquid crystal elastomer pendulum, *Int. J. Mech. Sci.* **227**, 107439 (2022).
- [54] P. Xu, H. Wu, Y. Dai, and K. Li, Self-sustained chaotic floating of a liquid crystal elastomer balloon under steady illumination, *Heliyon* **9**, e14447 (2023).
- [55] G. Vantomme, L. C. M. Elands, A. H. Gelebart, E. W. Meijer, A. Y. Pogromsky, H. Nijmeijer, and D. J. Broer, Coupled liquid crystalline oscillators in Huygens' synchrony, *Nat. Mater.* **20**, 1702 (2021).
- [56] G. Vantomme, A. H. Gelebart, D. J. Broer, and E. W. Meijer, A four-blade light-driven plastic mill based on hydrazone liquid-crystal networks, *Tetrahedron* **73**, 4963 (2017).
- [57] A. H. Gelebart, D. J. Mulder, M. Varga, A. Konya, G. Vantomme, E. W. Meijer, R. S. Selinger, and D. J. Broer, Making waves in a photoactive polymer film, *Nature (London)* **546**, 632 (2017).
- [58] A. Chakrabarti, G. P. T. Choi, and L. Mahadevan, Self-excited motions of volatile drops on swellable sheets, *Phys. Rev. Lett.* **124**, 258002 (2020).
- [59] K. M. Herbert, H. E. Fowler, J. M. McCracken, K. R. Schlafmann, J. A. Koch, and J. Timothy, White synthesis and alignment of liquid crystalline elastomers, *Nat. Rev. Mater.* **7**, 23 (2021).
- [60] S. Li, H. Bai, Z. Liu, X. Zhang, C. Huang, L. W. Wiesner, M. Silberstein, F. Robert, and R. F. Shepherd, Digital light processing of liquid crystal elastomers for self-sensing artificial muscles, *Sci. Adv.* **7**, eabg3677 (2021).
- [61] M. Wang, Z. Cheng, B. Zuo, X. Chen, S. Huang, and H. Yang, Liquid crystal elastomer electric locomotives, *ACS Macro. Lett.* **9**, 860 (2020).
- [62] J. Zhang, Y. Guo, W. Hu, R. H. Soon, Z. S. Davidson, and M. Sitti, Liquid crystal elastomer-based magnetic composite films for reconfigurable shape-morphing soft miniature machines, *Adv. Mater.* **33**, 2006191 (2021).
- [63] M. Parrany, Nonlinear light-induced vibration behavior of liquid crystal elastomer beam, *Int. J. Mech. Sci.* **136**, 179 (2018).
- [64] Y. Kim, J. Berg, and A. J. Crosby, Autonomous snapping and jumping polymer gels, *Nat. Mater.* **20**, 1695 (2021).
- [65] D. Zhao and Y. Liu, Photomechanical vibration energy harvesting based on liquid crystal elastomer cantilever, *Smart Mater. Struct.* **28**, 075017 (2019).
- [66] M. Knežević and M. Warner, Optomechanical elastomeric engine, *Phys. Rev. E* **88**, 040501 (2013).
- [67] K. Kumar, C. Knie, D. Bléger, M. A. Peletier, H. Friedrich, S. Hecht, D. J. Broer, M. G. Debije, and A. P. H. J. Schenning, A chaotic self-oscillating sunlight-driven polymer actuator, *Nat. Commun.* **7**, 11975 (2016).
- [68] A. Gelebart, G. Vantomme, E. Meijer, and D. Broer, Mastering the photothermal effect in liquid crystal networks: A general approach for self-sustained mechanical oscillators, *Adv. Mater.* **29**, 1606712 (2017).
- [69] G. Vantomme, A. H. Gelebart, D. Jan Broer, and E. W. Meijer, Self-sustained actuation from heat dissipation in liquid crystal polymer networks, *J. Polym. Sci. Pol. Chem.* **56**, 1331 (2018).
- [70] M. Saed and E. Terentjev, Siloxane crosslinks with dynamic bond exchange enable shape programming in liquid-crystalline elastomers, *Sci. Rep.* **10**, 6609 (2020).
- [71] X. Lv, M. Yu, W. Wang, and H. Yu, Photothermal pneumatic wheel with high loadbearing capacity, *Compos Commun.* **24**, 100651 (2021).
- [72] V. Domenici and B. Zalar, Paranematic-nematic phase transition in liquid crystalline elastomers: A2H-NMR study, *Phase Transit.* **83**, 1014 (2010).
- [73] M. Camacho-Lopez, H. Finkelmann, P. Palfy-Muhoray, and M. Shelley, Fast liquid-crystal elastomer swims into the dark, *Nat. Mater.* **3**, 307 (2004).
- [74] P. M. Hogan, A. R. Tajbakhsh, and E. M. Terentjev, UV manipulation of order and macroscopic shape in nematic elastomers, *Phys. Rev. E* **65**, 041720 (2002).
- [75] A. Baumann, A. Sánchez-Ferrer, L. Jacomine, P. Martinoty, V. Houerou, F. Ziebert, and I. Kulić, Motorizing fibers

- with geometric zero-energy modes, *Nat. Mater.* **17**, 523 (2018).
- [76] Q. He, Z. Wang, Y. Wang, Z. Wang, C. Li, R. Annapooranan, J. Zeng, R. Chen, and S. Cai, Electrospun liquid crystal elastomer microfiber actuator, *Sci. Robot* **6**, eabi9704 (2021).
- [77] Y. Wang, J. Sun, W. Liao, and Z. Yang, Liquid crystal elastomer twist fibers towards rotating microengines, *Adv. Mater.* **34**, 2107840 (2021).
- [78] See Supplemental Material at <http://link.aps.org/supplemental/10.1103/PhysRevE.109.034701> for two cases for the LCE engine; heat flux on the self-rotating LCE engine; contraction coefficient on self-rotating LCE engine; damping coefficient on the self-rotating LCE engine; spring constant on the self-rotating LCE engine; radius of turnplate on the self-rotating LCE engine; and initial velocity on the self-rotating LCE engine.